LAWRENCE
LIVERMORE
NATIONAL
LABORATORY

Investigation of the fragmentation of an explosively driven cylinder

C. W. Arthur , T. A. Dunn

January 12, 2015

Disclaimer

This document was prepared as an account of work sponsored by an agency of the United States government. Neither the United States government nor Lawrence Livermore National Security, LLC, nor any of their employees makes any warranty, expressed or implied, or assumes any legal liability or responsibility for the accuracy, completeness, or usefulness of any information, apparatus, product, or process disclosed, or represents that its use would not infringe privately owned rights. Reference herein to any specific commercial product, process, or service by trade name, trademark, manufacturer, or otherwise does not necessarily constitute or imply its endorsement, recommendation, or favoring by the United States government or Lawrence Livermore National Security, LLC. The views and opinions of authors expressed herein do not necessarily state or reflect those of the United States government or Lawrence Livermore National Security, LLC, and shall not be used for advertising or product endorsement purposes.

Investigation of the fragmentation of an explosively driven cylinder

Carly W. Arthur

12 September 2014

Disclaimer

Table of Contents

Table of Figures

Table of Equations

Table of Tables

Section 1

Motivation

1.1   Overview

The detonation of an explosively driven cylinder was simulated using three different methodologies within the multi-physics code of ALE3D. These computational methods are Lagrangian, Arbitrary-Lagrangian-Eulerian (ALE) and embedded (FEusion) grid. The methods are evaluated by a comparison to the published experimental data. Each simulation utilizes a statistical Johnson-Cook failure model [2].

- Published experimental data
- Different Methodologies
- Comparison of computerized simulations

Previous work includes D.M. Goto's research of an explosively driven cylinder field experiment discussed in Section 2 and private communication authored by Rich Becker and Mary Jane Graham detailing a simulation of an explosively driven cylinder using ALE3D [3].

1.1.1   Executive Summary

Explosively driven fragmentation is highly complex. To better understand the field detonation, different methodologies (Lagrangian (with a failure threshold in VisIt and element erosion), ALE and embedded grid) were simulated to provide a comparison to the experimental data through the utilization of fragment distributions and gross deformation metrics. Provided with the geometrical parameters and the results from the experimental data, the computer simulations were conducted after the successful writing of each input file.   Mesh refinement – a scalar multiplier applied to the mesh to refine the results – was then studied. The objective was to find a value that parallels the experimental results as the mesh can be refine indefinitely, theoretically. Various mesh resolution scales were simulated and the results graphically compared, using the damage and failure variables from a statistical Johnson Cook failure model, the number of fragments over time as well as time required for each simulation to run and number of processors utilized. The desired result is a calculated method to quantify the comparison being performed.

Section 2

Published Experimental Data

2.1   Published Experiment

The field detonation was preformed May of 2007 and the journal article by Goto, Becker, Orzechowski, Springer, Sunwoo and Syn, "Investigation of the fracture and fragmentation of explosively driven rings and cylinders" was published in September of 2009 [1]. This field experiment provided a basis for comparison of the computerized simulations. Measured data and results were employed as a check on the computer simulations.

2.1.1   Experimental Description

The geometrical parameters and the experimental results were utilized in the computerized simulations.

1. Geometrical Parameters
    a. Cylindrical geometry
    b. AISI 1018 Steel casing
        i. Table 1 (below)
    c. LX-17 main charge
    d. LX-10 booster (frustrum)
    e. RP-1 detonator
    f. Nominal length of 20.32 cm
    g. Outer diameter of 5.08 cm
    h. Wall thickness of 0.30 cm
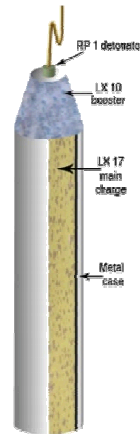
Figure 1 - Experimental configuration

The type of steel used was AISI 1018 steel and its material properties are summarized in Table 1.

Table 1 - Selected AISI 1018 steel properties.

AISI 1018 Steel Properties	
Density, (g/cm^3)	7.87
Sound speed, (longitudinal) (cm/µs)	0.577
Hardness	VHN$_{50}$135
Elastic modulus, (GPa)	195
Yield strength, (GPa)	0.24
UTS, (GPa)	0.436
Fracture strain, (quasistatic uniaxial tensile)	0.25

2. Experimental Diagnostics

The experiment was conducted in two fashions;

    a. Soft recovery preformed experiments to amass as many cylinder fragments as possible

        i. Surrounding the cylinder is an octagonal shaped box

            1. With 10.5 cm thick foam of density 0.32 g/cm^3

            2. Inside diameter of 95 cm and height of 61 cm (45 cm of air between cylinder and foam wall)

            3. Lid (25 cm thick) is placed on top of the foam box

            4. The foam box is placed within a 2.74 m diameter plastic tank filled with water to a depth of 60 cm
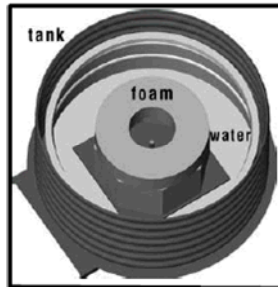
Figure 2 - Soft recovery experimental configuration.

Figure 3 - Cylinder steel fragments.

    b. Real time information was collected

        i. Using fast framing cameras, flash radiography and velocimetry of the steel

        ii. Velocimetry positions at z = 3.81 (P1), 7.62 (P2), 11.43 (P3), and 14.24 (P4) cm (z = 0 is the detonator end of the cylinder)
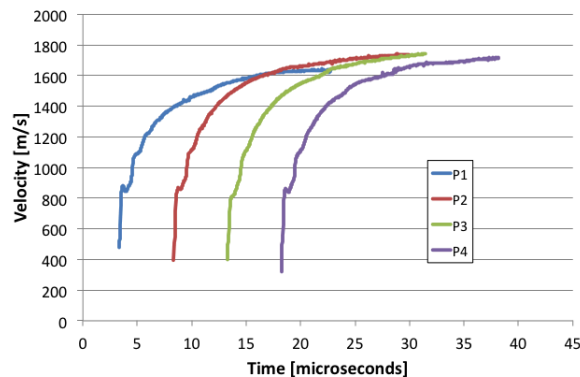
Figure 4 - Experimentally measured velocity of the cylinder.

2.1.1.1 *What's Next*

Even with the apparatus to catch each fragment in the soft capture series, 10 to 30 percent of the cylinder was not recovered. The next phase is to compare the published results to the ALE3D computerized simulations.

Section 3

ALE3D Computerized Simulations

3.1 Methodologies

The three methodologies employed for this field experimental reproduction were Lagrangian, Arbitrary-Lagrangian-Eulerian (ALE) and embedded (FEusion) grid. Each simulation utilized a statistical Johnson – Cook Failure model (equation shown below). Lagrangian and ALE employed the use of void seeding (approximation of material flow through failed regions). Embedded grid made use of element erosion (once an element has failed, it is deleted from the calculations). Lagrangian investigated the benefits of using element erosion in the simulated calculations.

$$\epsilon_f^n = [D_1 + D_2 \exp(D_s \sigma^*)][1 + D_4 \ln \dot{\epsilon}^*][1 + D_5 T^*]$$

$$Where\ D_{1,2,3,4\,\&5} = \sum_n \frac{\Delta \epsilon^n}{\epsilon_f^n}, \ \dot{\epsilon}^* = \frac{\dot{\epsilon}}{\dot{\epsilon}_0} \ and \ \sigma^* = -\frac{\sqrt{\frac{3}{2}\sigma_{ij}'\sigma_{ij}'}}{p}$$

Equation 1 - Statistical JC failure model.

3.1.1 Explanation

The objective was a measure of the accuracy of each method to the experimental data. This took into consideration composing the input files, run time and output precision.

1. Lagrangian
    a. Mesh moves at material velocity
    b. Mathematically accurate representation
    c. Mesh can tangle
    d. Mixed zones for not occur
        i. Maintains material interfaces
    e. Product gases cannot escape
    f. Used void seeding
    g. Employed element erosion as a comparison within Lagrangian framework
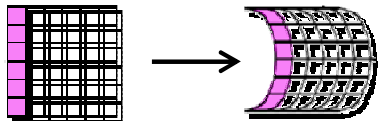
Figure 5 - Lagrangian movement

2. ALE
   a. Mesh movement is distinct from material velocity
   b. Combination of Lagrangian and Eulerian phases
   c. Includes a relaxation and advection stage
   d. Mesh will not tangle
      i. As mesh permits material to move through
   e. Allows for product gases to escape
   f. Used void seeding
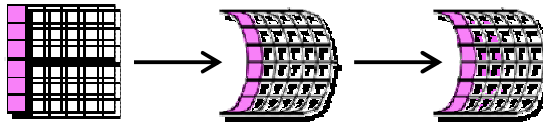
Figure 6 - ALE movement.

3. Embedded Grid

   a. Stipulated two geometrical meshes
      i. Background fluid mesh
      ii. Foreground Lagrangian mesh
   b. Better control over the parameters within the simulation
      i. Material has independent movement '
   c. Steel casing is the Lagrangian foreground
   d. Explosive and ambient air is the background fluid mesh
   e. Used element erosion

■ = Material
☐ = Foreground Mesh
☐ = Background Mesh

Figure 7 - Embedded grid movement.

3.1.1.1 *What's Next*

Each input file was ran and debugged until the output qualitatively matched a field detonation. The resolution scale factor for the geometrical mesh is increased until the output converges. This process is known as mesh resolution.

Section 4

Geometric Mesh Resolution Studies

4.1   Mesh Resolution

The resolution scale factors were doubled each run and are as follows; 1, 2, and 4 (where a factor of 1 is the initial set of geometrical mesh parameters). The visualization software of VisIt is then utilized as shown in Figure(s) 5 – 8 to visually view the results. Each image below is at twenty-three (23) micro-seconds for resolutions scales of 1, 2, 4, 8 and 16.
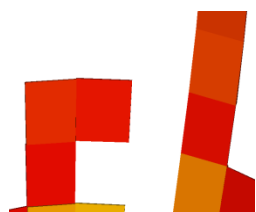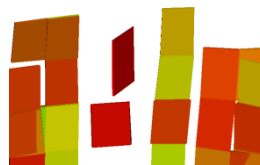
Figure 8 - Scale 1.   **Figure 9 - Scale 2.**   **Figure 10 - Scale 4.**   **Figure 11 - Scale 8.**   **Figure 12 - Scale 16.**
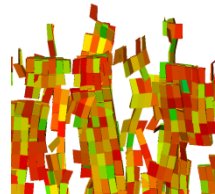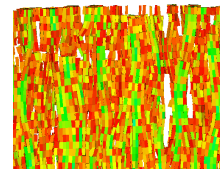
4.1.1   Purpose

Finer mesh resolution will yield an increase in the accuracy of the computerized results, to a certain extent. The objective is to compare the output from each scale resolution and the results will converge. Each of the three methodologies underwent mesh resolution studies. The results are visually compared as well as numerically by studying the fragment distributions. Below is an image of the field experimental detonation at 23 micro seconds.

Figure 13 – Experimental detonation at 23 micro-seconds.

a. Visual Comparison (comparing VisIt images at 23 micro-seconds:

1. Lagrangian (with a JC Failure Threshold in VisIt)
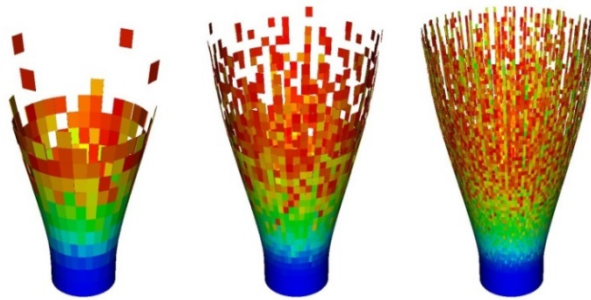
Figure 14 – Scale 1.   **Figure 15 – Scale 2.**   **Figure 16 – Scale 4.**

2. Lagrangian (with an element erosion input into the code)
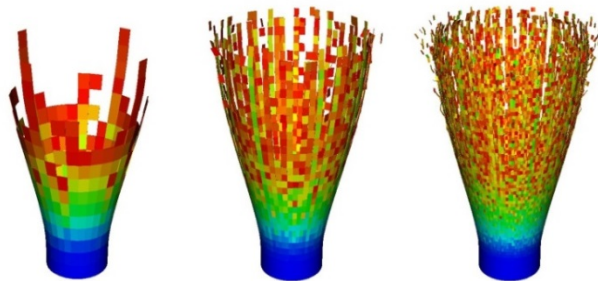
Figure 17 – Scale 1.   **Figure 18 – Scale 2.**   **Figure 19 – Scale 4.**

3. ALE (with a JC Failure Threshold in VisIt)
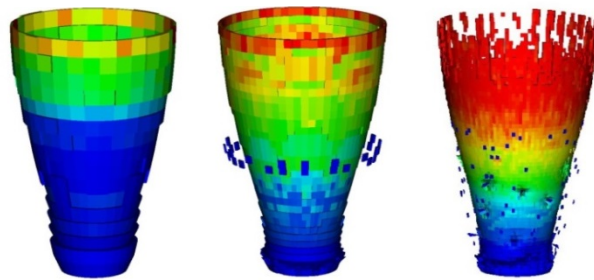
Figure 20 – Scale 1.   **Figure 21 – Scale 2.**   **Figure 22 – Scale 4.**

4. Embedded Grid (with an element erosion input into the code)
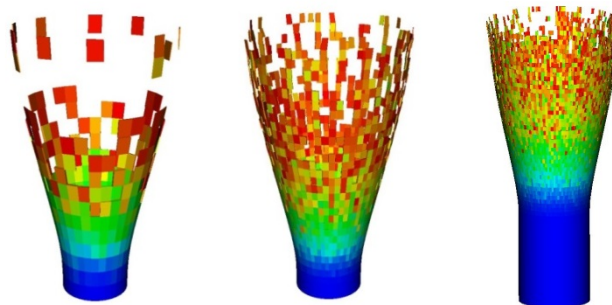
Figure 23 - Scale 1.   **Figure 24 - Scale 2.**   **Figure 2 - Scale 4 (at 17 μs).**

b. Numerically (comparing the number of fragments VisIt identified at 23 micro-seconds through an increase of mesh resolution scale)

1. Lagrangian (with a JC Failure Threshold in VisIt)

Lagrangian with Failure Threshold
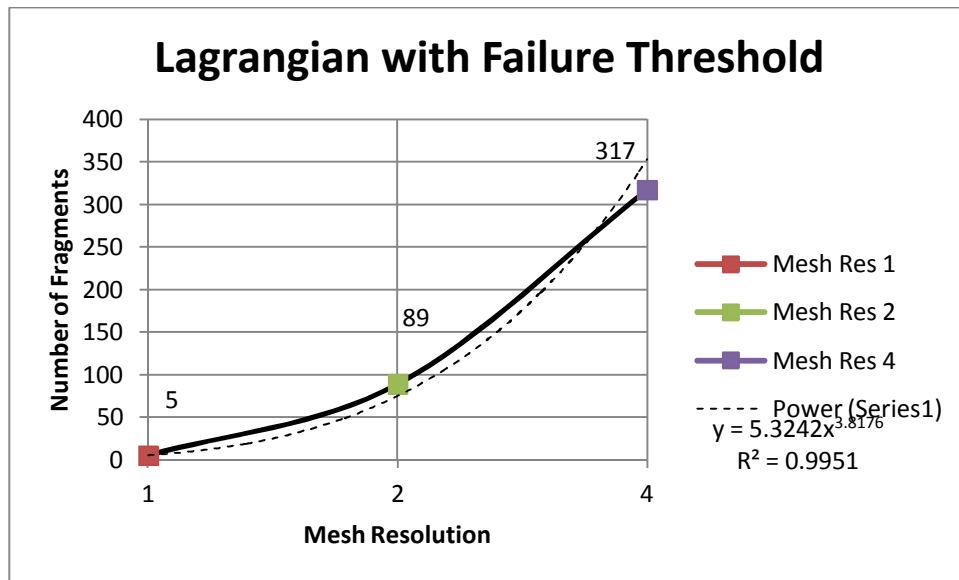
Figure 26 - Number of fragments found at 23 micro-seconds for each Lagrangian mesh resolution.

$y = 5.3242x^{3.8176}$
$R^2 = 0.9951$

2. Lagrangian (with an element erosion input into the code)

Lagrangian with Element Erosion

$y = 12.508x^{2.7726}$
$R^2 = 0.9965$
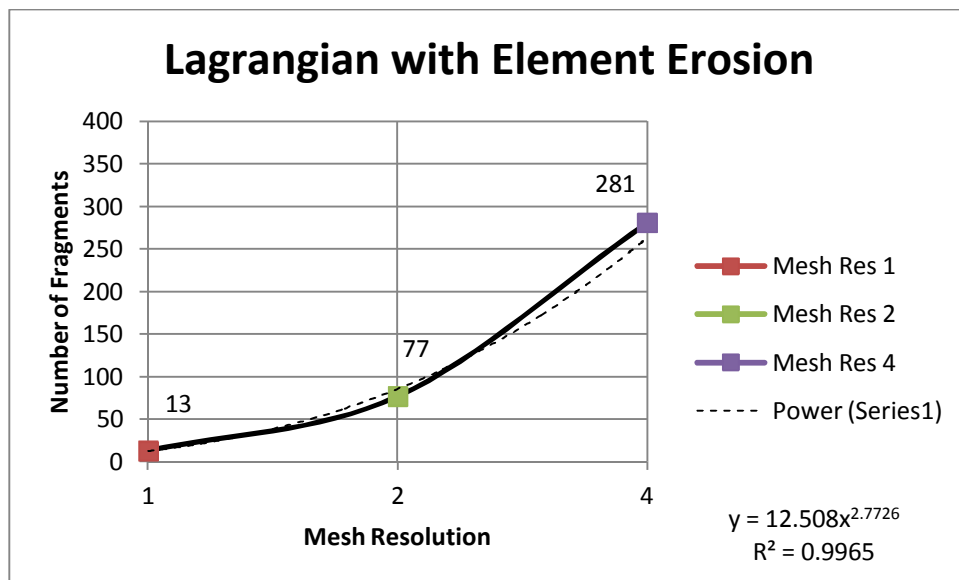
Figure 27 - Number of fragments found at 23 micro-seconds for each Lagrangian with element erosion mesh resolution.

3. ALE (with a JC Failure Threshold in VisIt)
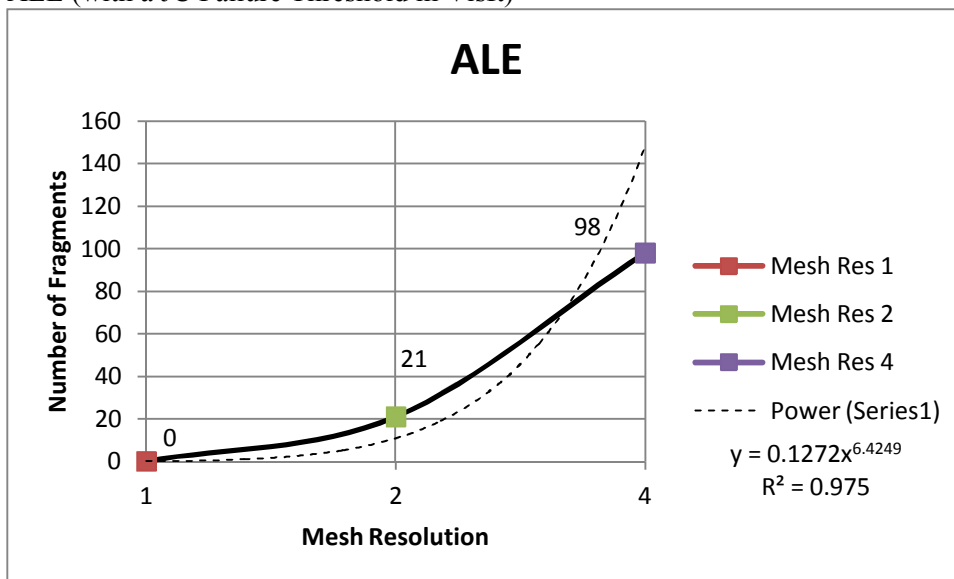
Figure 28 - Number of fragments found at 23 micro-seconds for each ALE mesh resolution.

4. Embedded Grid (with an element erosion input into the code)
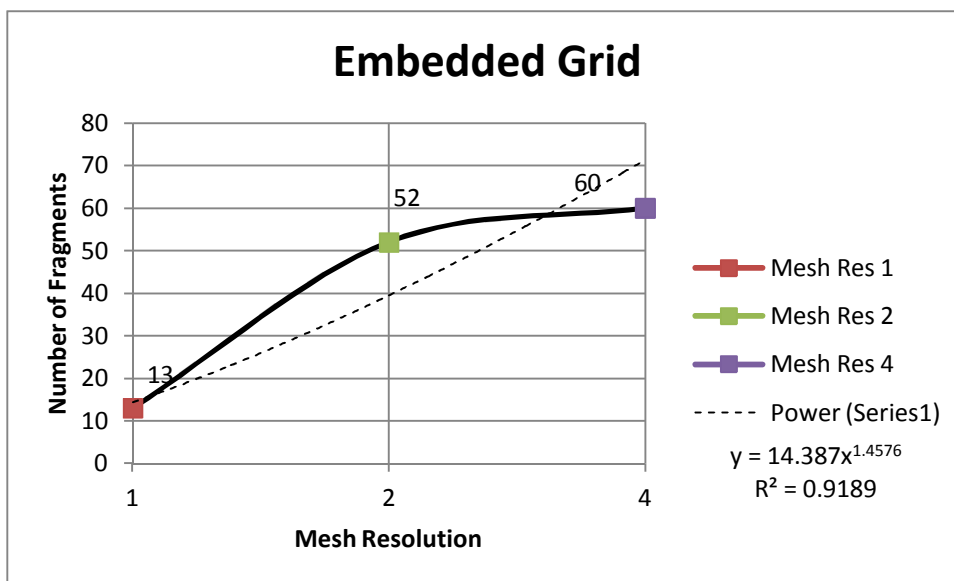
Figure 29 - Number of fragments found at 23 micro-seconds for each embedded grid mesh resolution.

Embedded grid, resolution 4 ran to 17 micro-seconds, results up to that time are shown here

4.1.2   Explanation

Conceptually, doubling the scale each run effectively halves the length scale in the simulation thusly refining it as a multiple of two from the previous run. Ideally, a convergence in the mesh scale resolutions is the desired output. This can be determined by a visual approach using the Johnson Cook failure model of the steel material, graphically produced in Microsoft Excel.

Graphs of the average mass of the failed steel material are plotted against the time in micro-seconds to achieve a function that differs in line path as the mesh resolution is increased. According to these graphical presentations, the mesh resolution converges to a scalar quantity.

The simulated cases which employed the use of element erosion could not be graphed with the JC failure parameter. Instead, a timehist of the 'zmass' sum in region 2 (steel) was used. Manually determining the averages was completed by taking the difference of the total mass at timestep 0 and each subsequent timestep after, and then dividing by the initial mass to yield the failed steel material expressed as a percentage. This process was used in Lagrangian with element erosion and embedded grid.

1. Lagrangian (with a JC Failure Threshold in VisIt)
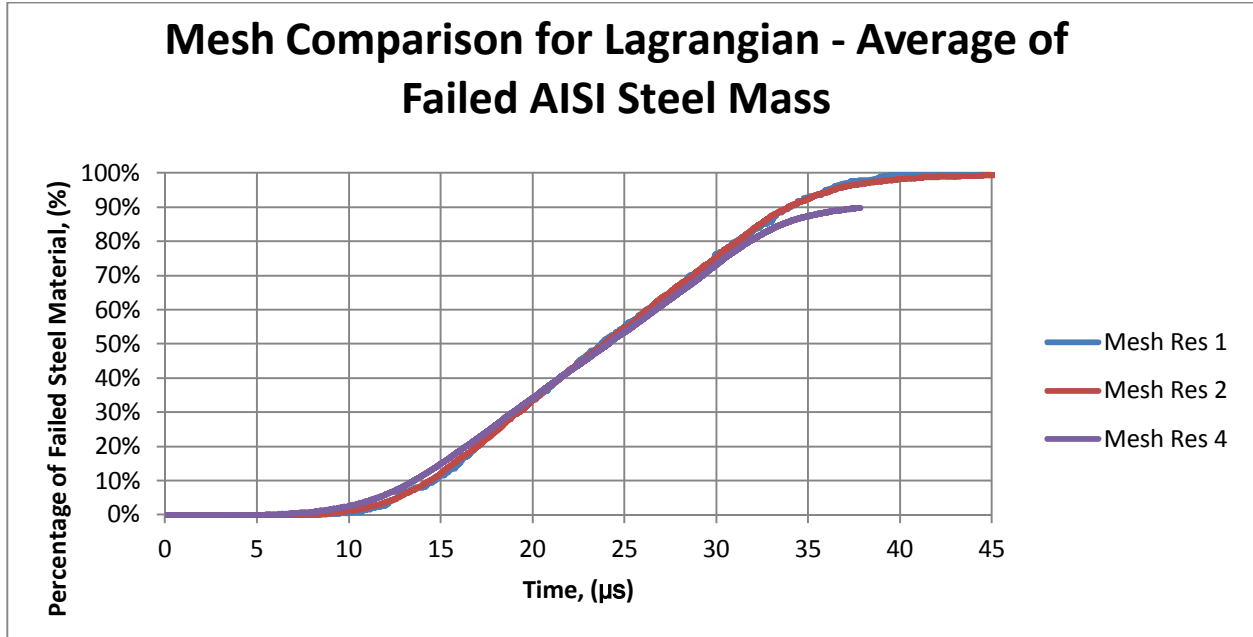
Figure 30 - Lagrangian with failure threshold in VisIt mesh resolution comparison using failed steel mass.

2. Lagrangian (with an element erosion input into the code)
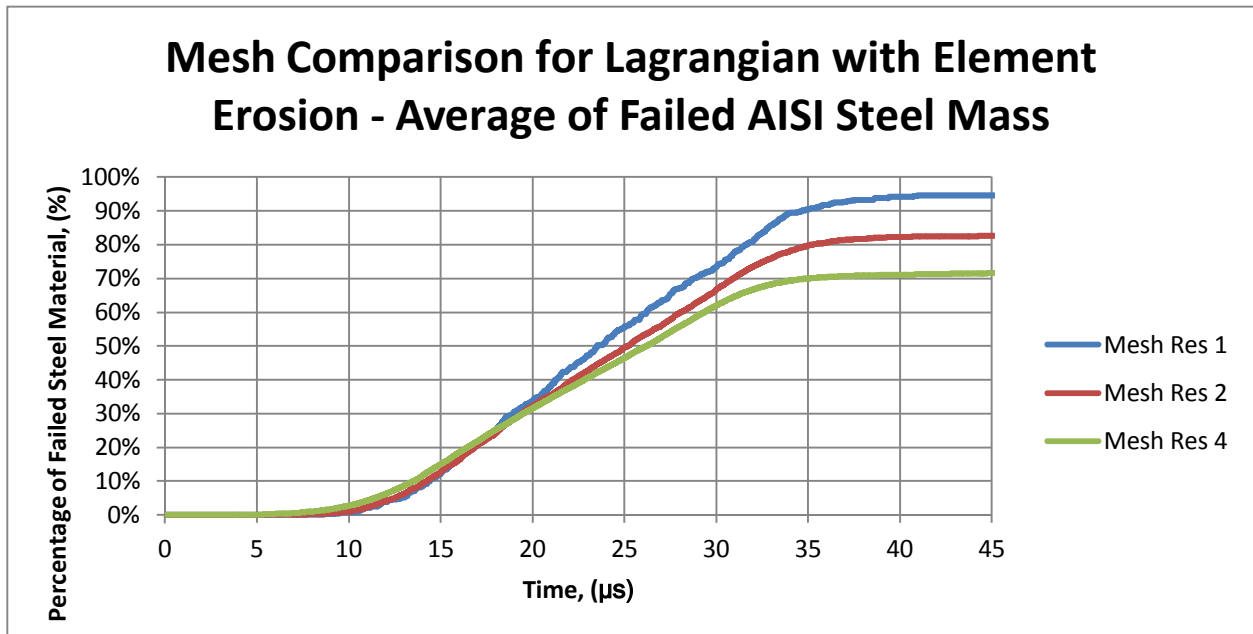
Figure 31 - Lagrangian with element erosion mesh resolution comparison using failed steel mass.

3. ALE (with a JC Failure Threshold in VisIt)
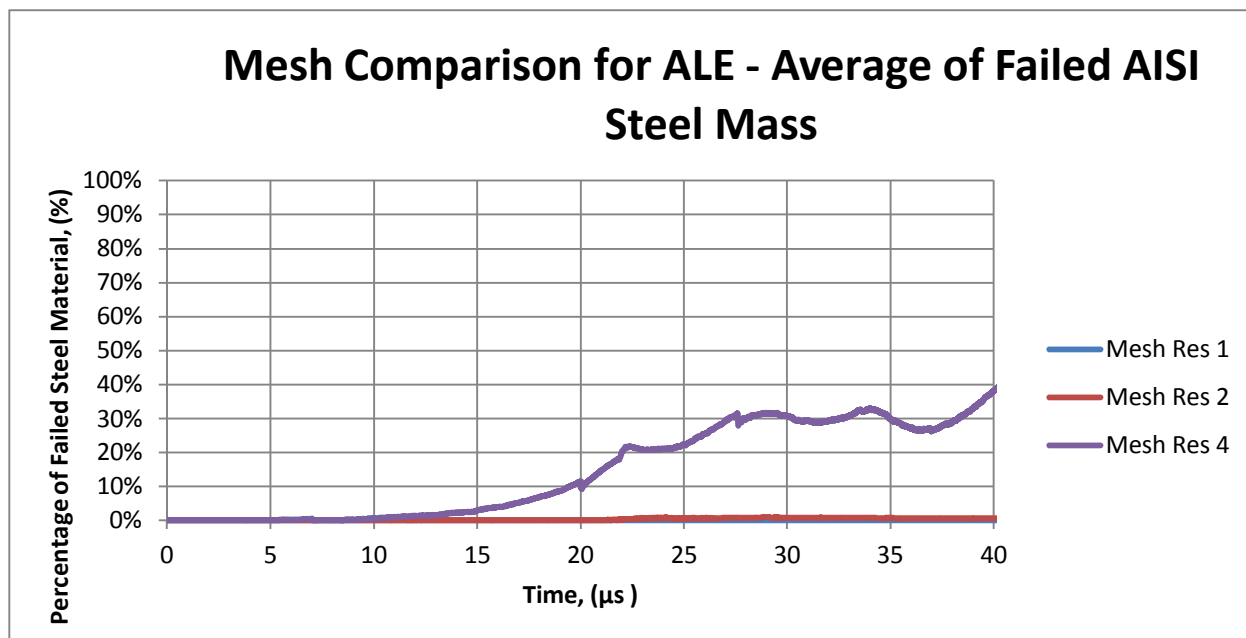
Figure 32 - ALE mesh resolution comparison using failed steel mass.

4. Embedded (with an element erosion input into the code)
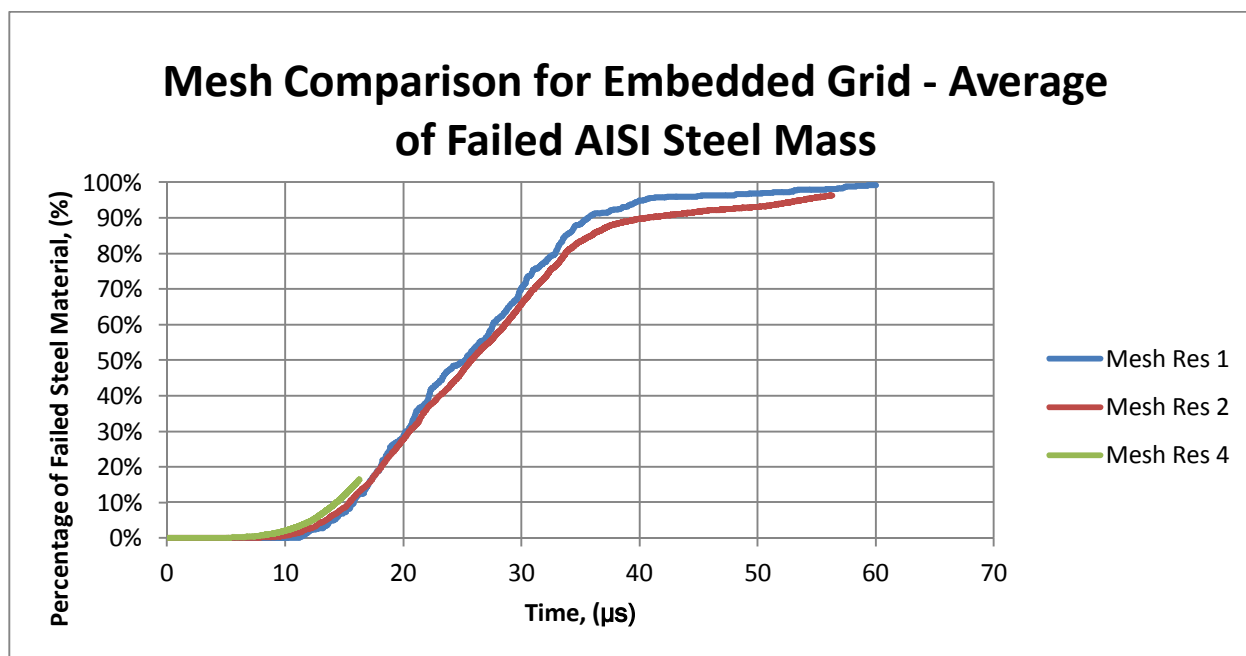
Figure 33 - Embedded grid mesh resolution comparison using failed steel mass.

Embedded grid, resolution 4 ran to 17 micro-seconds, results up to that time are shown here

4.1.2.1 What's Next

The mesh resolutions did not converge as seen by Figures 30 through 33 above. This effect may be mitigated through increasing the mesh resolution scale factor. Each initial input file maintained its written integrity however, as the mesh scale of refinement increased, differing issues were generated by the code. The result was the input file for each simulated run changed slightly in the initializing of certain commands (ie, advection and hydro parameter blocks). A more in depth look at the mesh resolution can better assure the mathematical accuracy. Investigation into how the mesh resolutions of the computerized simulations effect the fragmentation distribution is the next phase.

Section 5

Simulation Results & Post Processing

5.1 Fragmentation Distributions

Using the visualization software of VisIt and its Python Interface, the amount of fragments was queried from each simulation and the results presented graphically. Below is a figure depicting the results of Becker and Graham's research using ALE3D hydrocode, VisIt and post processing with a Python script. The method employed by Becker and Graham is ALE employing a statistical Johnson Cook failure model with Weibull probability distribution function and void seeding.
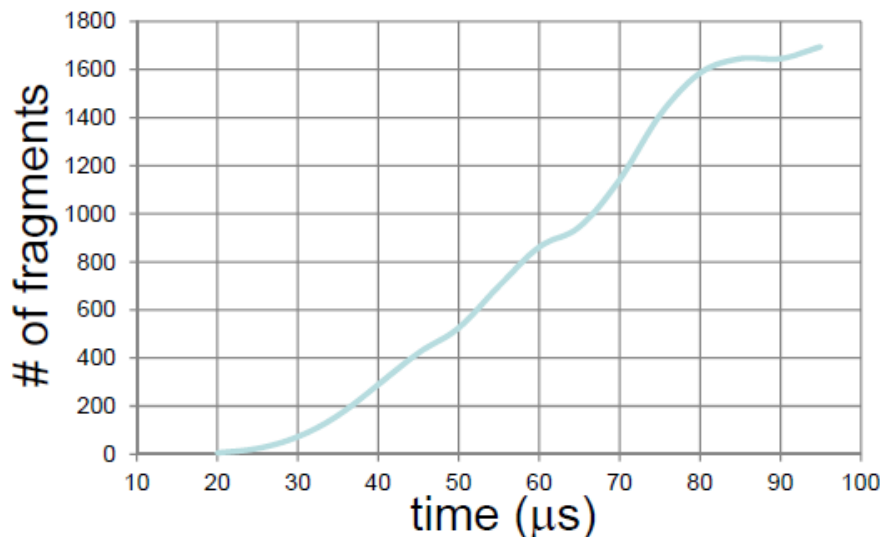
Figure 34 - Fragment results from R. Becker and M.J Graham's research [3].

5.1.1 Explanation

Utilizing the fragmentation distributions and the gross deformation metrics provided a technique to compare the simulation results to those of the field experiment. Macros were written using VisIt's Python Interface (a basis of the Python language) and then utilized in querying both the Time and Number of Connected Components (fragments).

1. Lagrangian (with a JC Failure Threshold in VisIt)
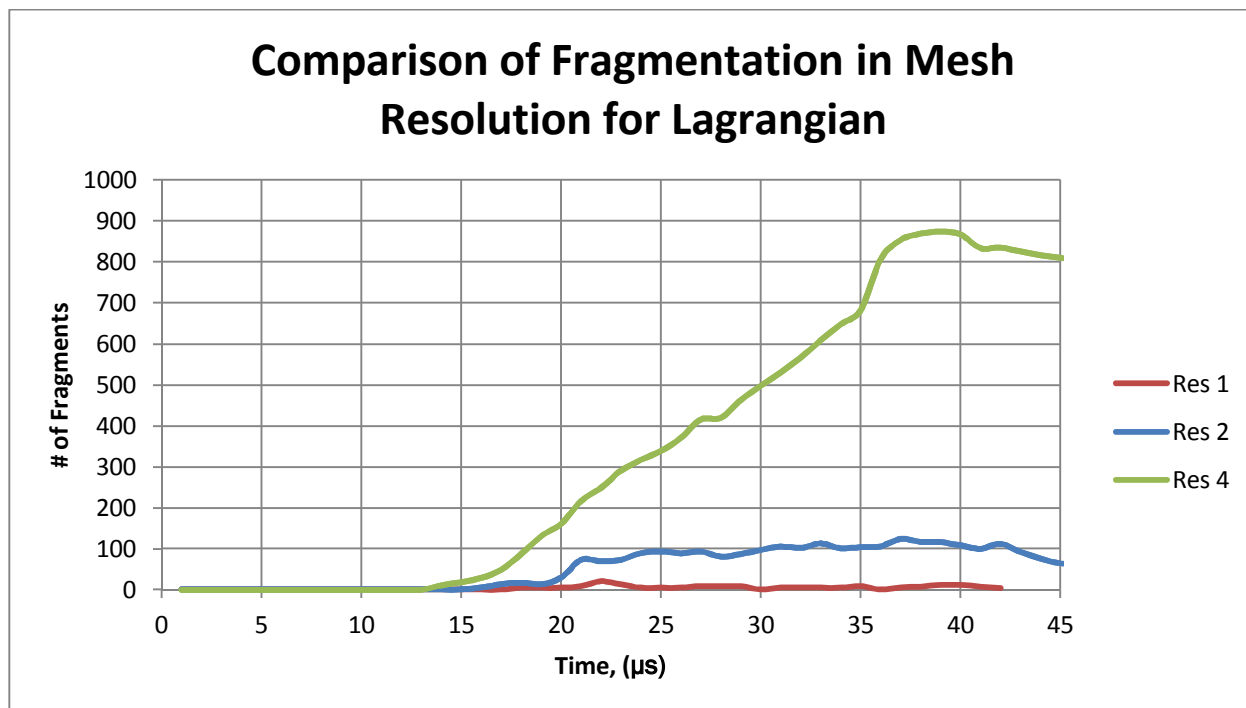
Figure 35 - Fragment distribution for Lagrangian with a failure threshold.

2. Lagrangian (with an element erosion input into the code)
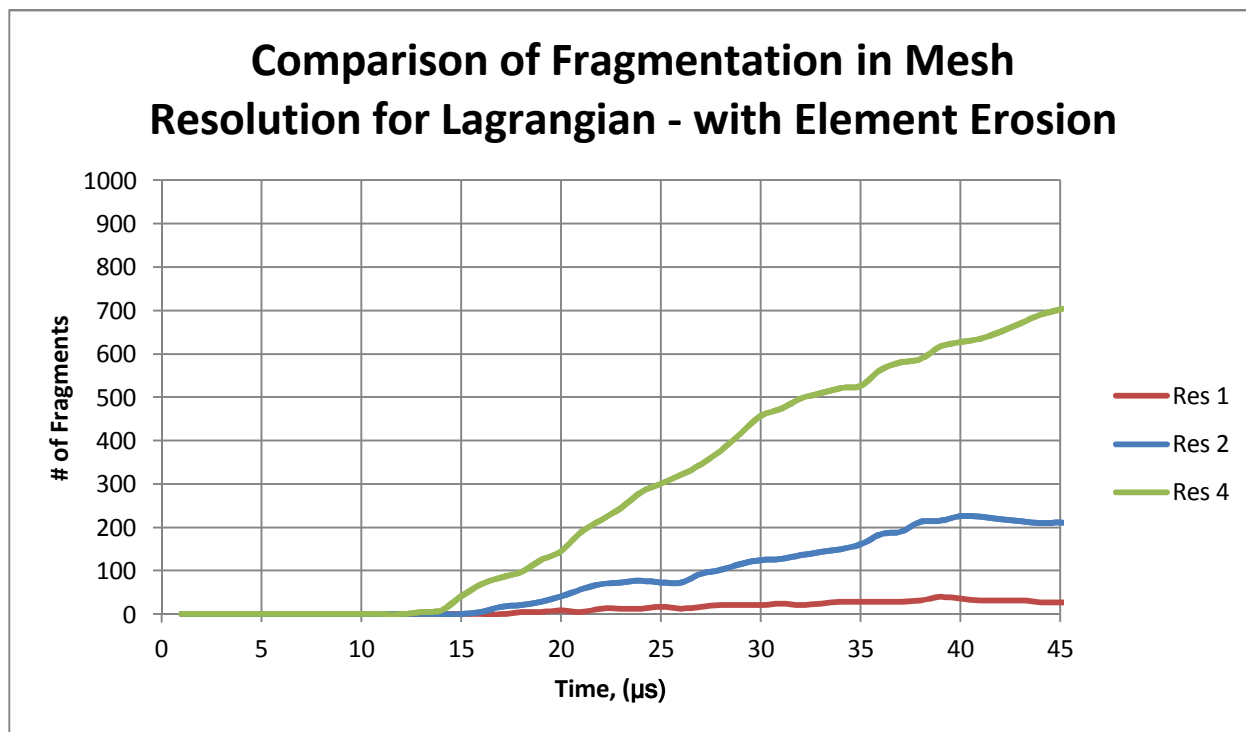
Figure 36 - Fragment distribution for Lagrangian with element erosion.

3. ALE (with a JC Failure Threshold in VisIt)
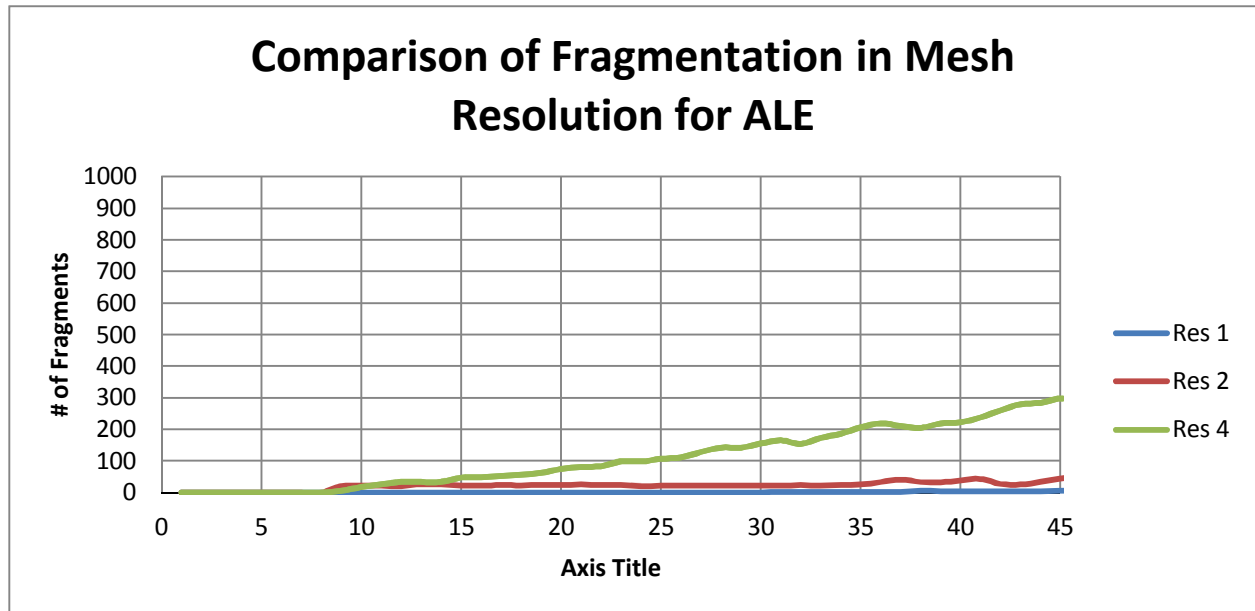
Figure 37 - Fragment distribution for ALE with a failure threshold.

4. Embedded grid (with an element erosion input into the code)
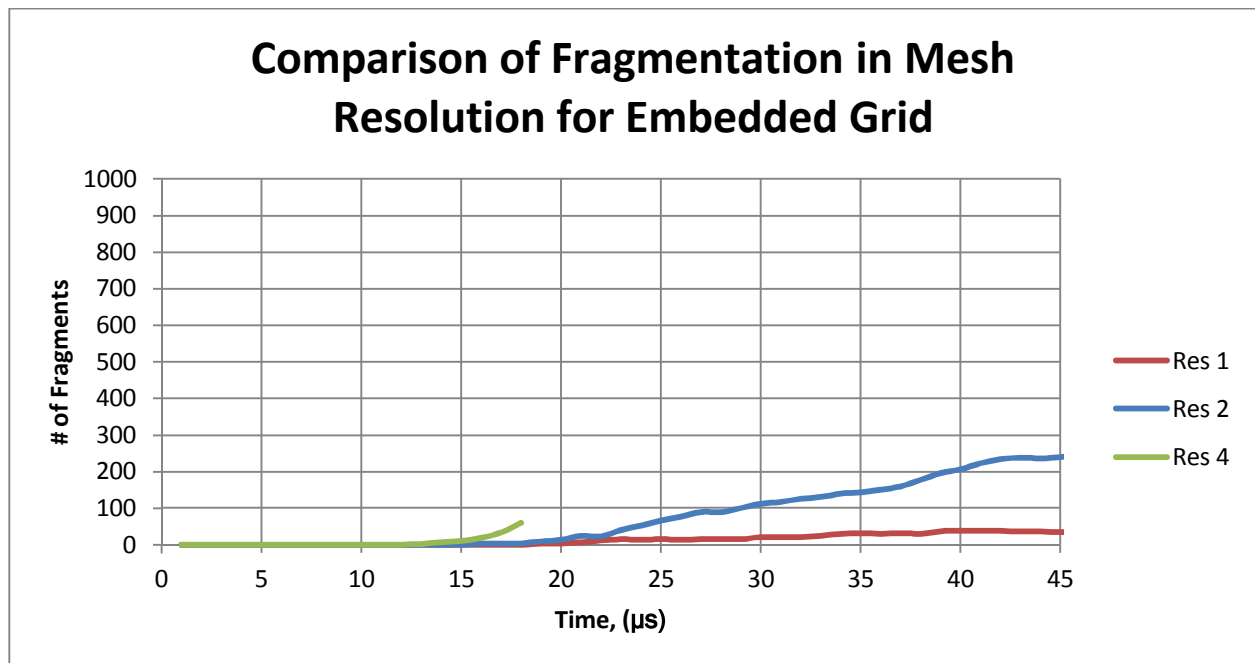
Figure 38 - Fragment distribution for embedded grid with element erosion.

Embedded grid, resolution 4 ran to 17 micro-seconds, results up to that time are shown here

5.1.1.1 *What's Next*

Each figure represents the amount of fragments over time that VisIt queried for each mesh resolution scale. Further mesh resolution can be conducted to better refine the mathematical accuracy of the simulated results.

5.2   Gross Deformation Mechanics

In the series of experiment where real time information was collected, the results of the field experiment can be compared to those of the computer simulations. The field experiment used fast framing cameras, flash radiography and velocimetry to depict the behavior of the AISI 1018 steel before, during and after detonation. The velocimetry probes were positioned at z = 3.81 (P1), 7.62 (P2), 11.43 (P3), and 14.24 (P4) cm where detonation occurred at z = 0.
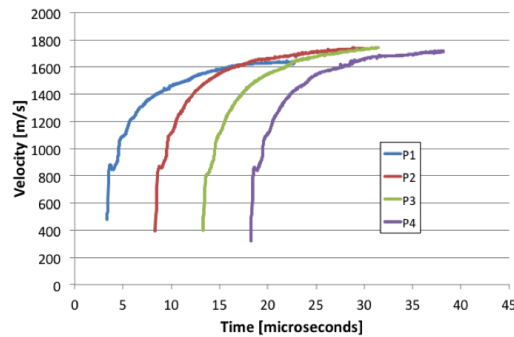
Figure 39 - Experimentally measured velocity of the cylinder.

5.2.1   Explanation

Comparing the velocity of the field experiment and the results of the computerized simulations provides a 'real life' evaluation. Speed and velocity are simple concepts to practically grasp and allow an experimental justification to the validity of the simulated results.

Utilizing timehistory variables written in the input files, tracer particles were placed on the steel casingto monitor the speed in each location (P1, P2, P3 and P4). The data was recorded and presented graphically in Microsoft Excel. The mesh resolution scales 1, 2 and 4 are shown here for comparison purposes.

1. Lagrangian (with a JC Failure Threshold in VisIt)
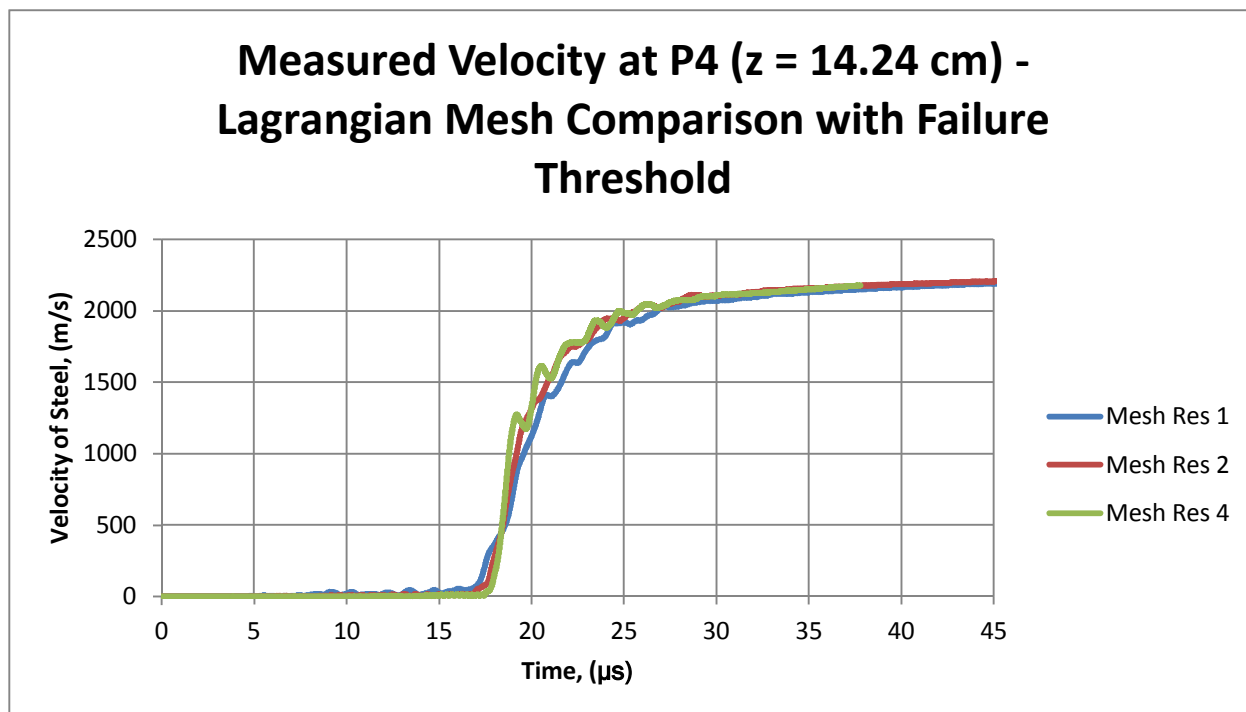
Figure 40 - Velocity comparison for different mesh resolutions Lagrangian with failure threshold.

2. Lagrangian (with an element erosion input into the code)
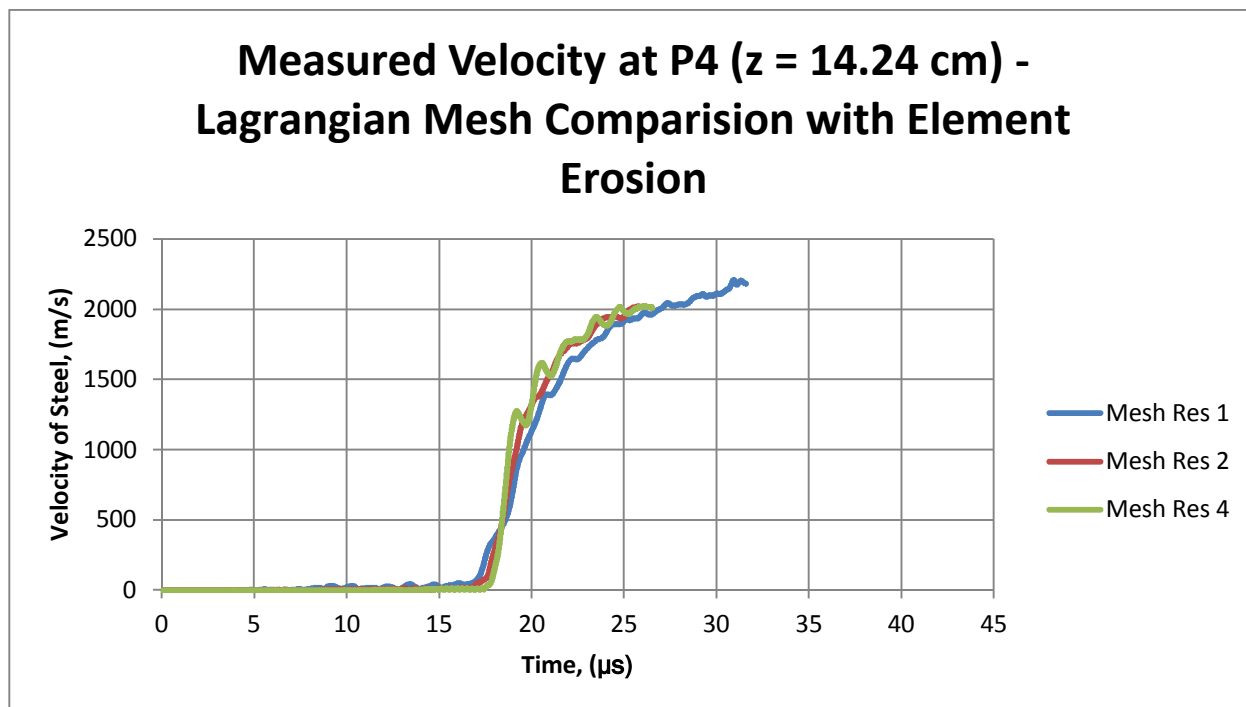
Figure 41 - Velocity comparison for different mesh resolutions Lagrangian with element erosion.

3.   ALE (with a JC Failure Threshold in VisIt)

Measured Velocity at P4 (z = 14.24 cm) - ALE Mesh Comparison
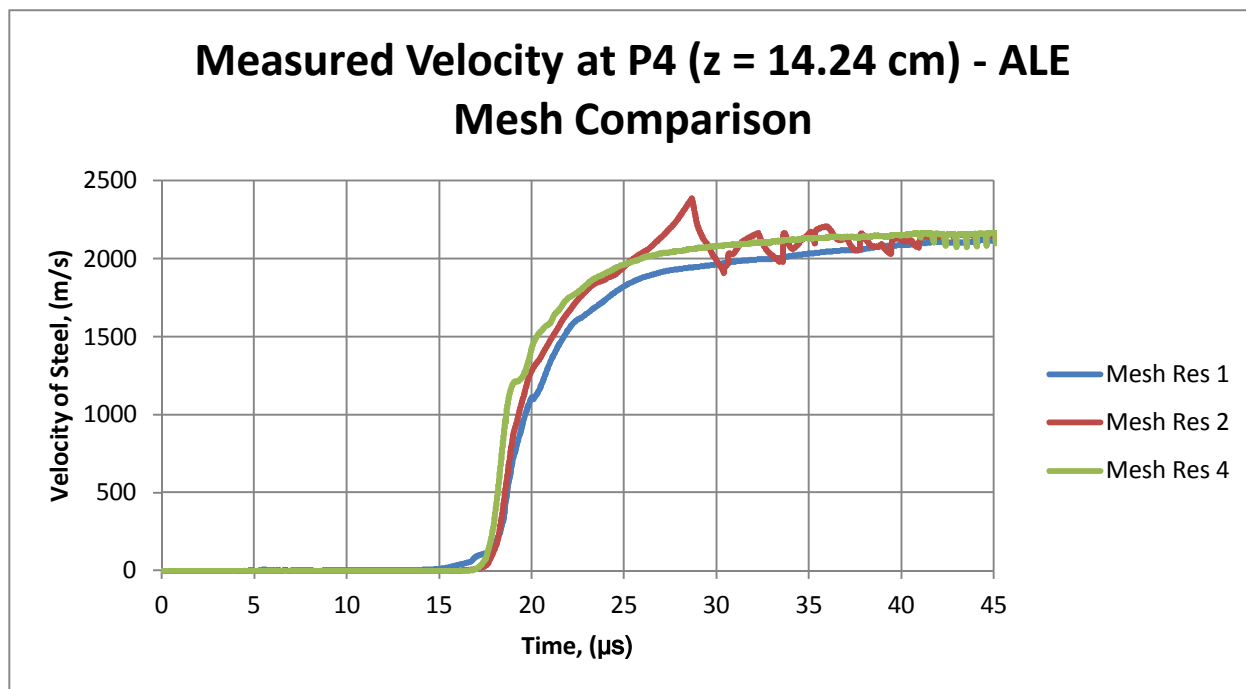
Figure 42 - Velocity comparison for different mesh resolutions ALE.

4.   Embedded grid (with an element erosion input into the code)

Measured Velocity at P4 (z = 14.24 cm) - Embedded Grid Mesh Comparison
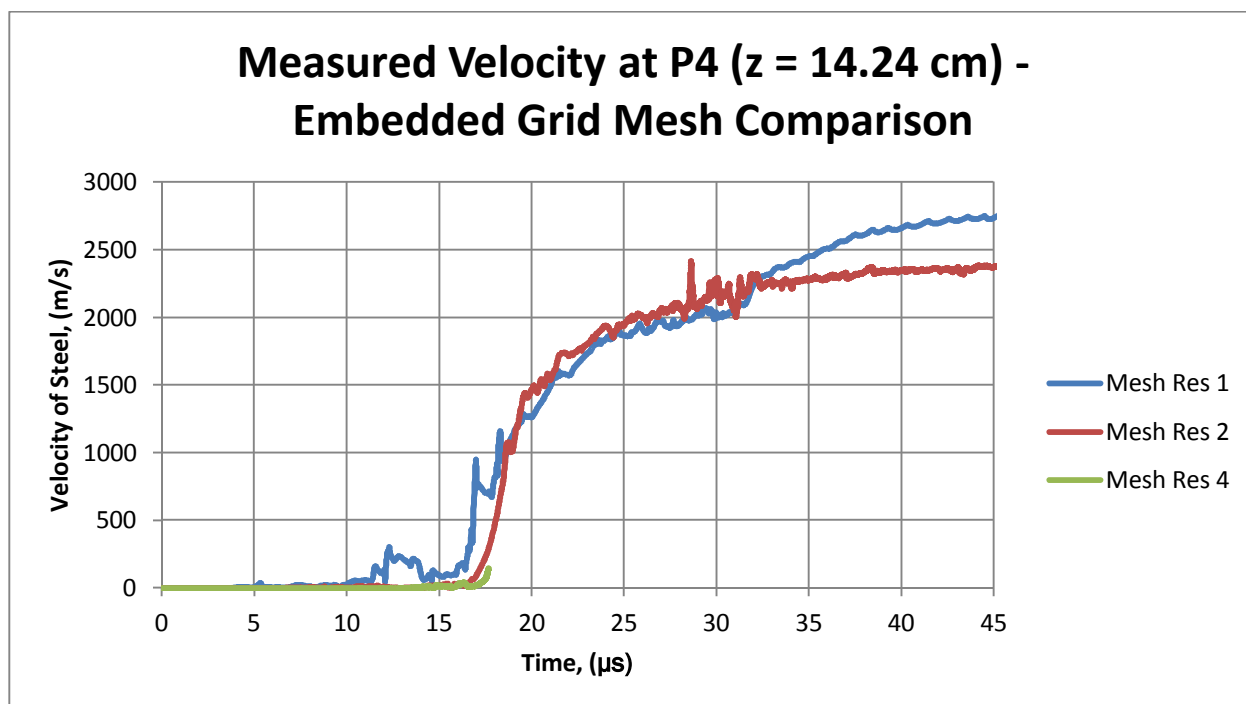
Figure 3 - Velocity comparison for different mesh resolutions embedded grid.

Embedded grid, resolution 4 ran to 17 micro-seconds, results up to that time are shown here

5.2.1.1 *What's Next*

Comparing the selected mesh resolution scale factor velocity figure to those of the experimental velocimetry probes provides a way to validate each method (Lagrangian (element erosion and failure threshold), ALE and embedded grid. Further research behind the physics of the detonation and expansion of the cylinder can be investigated. Examples of this can be why the velocity figures plot the functions shown and how the jumps and drops of the graphs can be explained.

Section 6

Conclusions & Future Work

6.1 Conclusion

Another factor to take into consideration is the practicality of each method. This can be determined by a comparison between run time and number of processors require for each simulation.

Table 2 - Summary of simulation logistics.

Logistics Comparison		Res 1	Res 2	Res 4
Lagrangian (with failure threshold)	Time, (sec)	26.104	171.596	1820.005
	Time, (min)	0.435	2.860	30.333
	Time, (hr)	0.007	0.048	0.506
	Nodes	1	1	8
	Processors	16	16	64
Lagrangian (with element erosion)	Time, (sec)	76.552	141.117	1297.548
	Time, (min)	1.276	2.352	21.626
	Time, (hr)	0.021	0.039	0.360
	Nodes	3	3	3
	Processors	48	48	48
ALE	Time, (sec)	48.635	598.501	7271.734
	Time, (min)	0.811	9.975	121.196
	Time, (hr)	0.014	0.166	2.020
	Nodes	1	1	3
	Processors	16	16	48
Embedded Grid	Time, (sec)	1885.857	39995.472	56986.304
	Time, (min)	31.431	666.591	949.772
	Time, (hr)	0.524	11.110	15.830
	Nodes	3	8	8
	Processors	48	48	64

Embedded grid, resolution 4 ran to 17 micro-seconds, results up to that time are shown here

Further mesh resolution studies can be continued as the issues in the input files which caused the code to abort are resolved. One the issues that arose was the error message of "Too much advection" in the ALE

calculations. It is the belief that the high explosive (LX-17) core was more refined than that of the coarse air outside the outer steel casing. Due to this discrepancy in refinement, the HE streamed through the steel and air in the later timesteps. An image depicting this phenomenon is shown below, displaying the HE pushing through as well as the mesh tangling near the bottom of the cylinder.
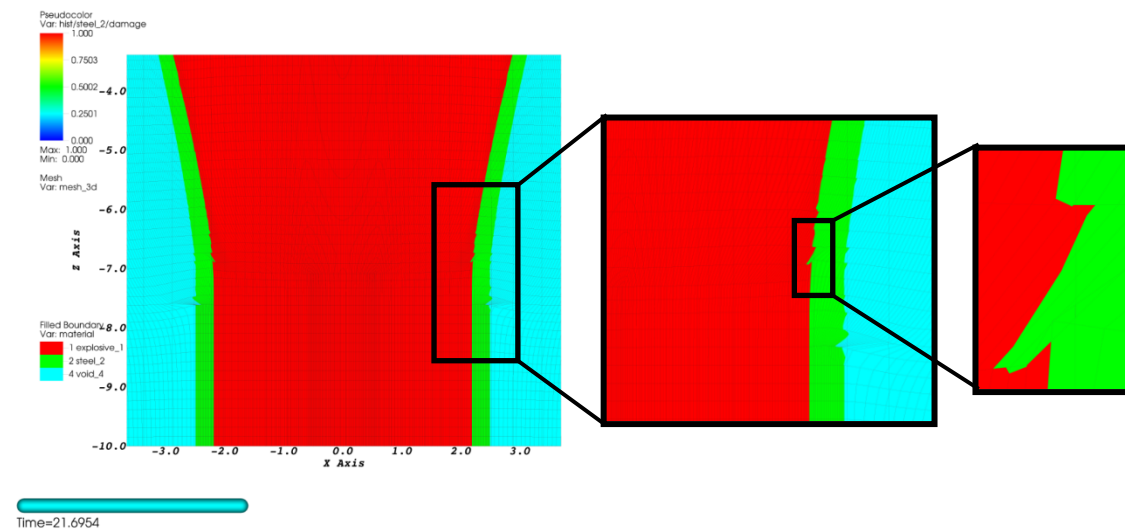

Figure 44 - VisIt plot of HE streaming through the steel and air mesh.

6.1.1   Future Work

Steps to resolve this advection problem could be refining the air mesh and adjusting the advection parameters in both the advection and region parameter blocks. To refine the coarse air mesh, the geometrical parameters of the mesh should be adjusted to minimize the difference in mesh scaling between the HE core and the ambient air. Commands such as 'rlxholduntil' (allows no advection to a specific nodeset until a certain time) and 'rlxholdinactive' (allows no relaxation to a specific nodeset until a certain time in which the nodeset become active) within the advection block can help delay the advection of the HE. The command of 'rxldxmnf' can be decreased which limits nodal movement to fix the advection to a fixed length.

6.1.1.1   What's Next

Quantitative comparisons between the field experiments and the computerized simulations would be the next desired output. Numerical justification would increase the validity of the simulations, while the qualitative results shown in the report provide a visual comparison.

6.1.2   Acknowledgments

The author would like to thank Lawrence Livermore National Laboratory for the opportunity of a summer student internship, D.M. Goto for the published field experimental results, Rich Becker and Mary Jane Graham for the presentation of explosively driven cylinder using ALE3D. A special thanks to mentor, Tim Dunn with help from Sam Schofield. Chad Noble, Andy Anderson and Rose McCallen were also instrumental in this process.

6.2 References

[1]   Goto, D.M, Becker, R., Orzechowski, H.K. Springer, A.J. Sunwoo, C.K. Syn, Investigation of the Fracture and Fragmentation of Explosively Driven Rings and Cylinders, *Int. J. Impact Eng.*, **35**-12, 2008.

[2]   G. R. Johnson and W. H. Cook. Fracture characteristics of three metals subjected to various strains, strain rates, temperatures, and pressures. *Engineering Fracture Mechanics*, **21**:31–48, 1985.

[3]   R. Becker, M.J. Graham, ARL Laboratory, private communication.